NANOMATERIALS

Seeded 2D epitaxy of large-area single-crystal films of the van der Waals semiconductor 2H $MoTe_2$

Xiaolong Xu[1,2], Yu Pan[1], Shuai Liu[1], Bo Han[3,4], Pingfan Gu[1], Siheng Li[4], Wanjin Xu[1], Yuxuan Peng[1], Zheng Han[5,6], Ji Chen[1], Peng Gao[2,3,4], Yu Ye[1,2,7]*

The integration of two-dimensional (2D) van der Waals semiconductors into silicon electronics technology will require the production of large-scale, uniform, and highly crystalline films. We report a route for synthesizing wafer-scale single-crystalline 2H molybdenum ditelluride ($MoTe_2$) semiconductors on an amorphous insulating substrate. In-plane 2D-epitaxy growth by tellurizing was triggered from a deliberately implanted single seed crystal. The resulting single-crystalline film completely covered a 2.5-centimeter wafer with excellent uniformity. The 2H $MoTe_2$ 2D single-crystalline film can use itself as a template for further rapid epitaxy in a vertical manner. Transistor arrays fabricated with the as-prepared 2H $MoTe_2$ single crystals exhibited high electrical performance, with excellent uniformity and 100% device yield.

Two-dimensional (2D) semiconductors, such as MoS_2 (*1*) and black phosphorus (*2*), could compete with silicon technology because of their atomic thickness (*1*, *3*), excellent physical properties (*2*, *4*–*6*), and compatibility with classic complementary metal-oxide semiconductor (CMOS) technologies (*7*, *8*). A prerequisite for achieving large-scale integrated circuits made of 2D semiconductors is the mass production of their raw materials with high quality and uniformity (*9*, *10*). Silicon wafers are obtained by cleaving bulk ingots of Si single crystals, whereas large-area 2D semiconductors are usually obtained through bottom-up deposition methods (*11*–*14*). Flaws such as grain boundaries and crystallographic defects introduced during growth often lead to severe degradation of electronic performance (*15*). Wafer-scale single-crystalline 2D semiconductors on insulating substrates are highly desired, but their growth remains extremely challenging.

Most methods for preparing bulk single crystals cannot be adopted for synthesizing large-sized 2D semiconductor single crystals, because the atomic thickness of 2D materials makes their synthesis strongly dependent on the surface properties of the substrates (*10*, *16*). For example, transforming a polycrystalline 2D thin film into a single crystal only by thermal annealing must overcome the high energy barrier of rotating a 2D crystal domain on a substrate (*17*). Recently, graphene, a single-crystalline 2D semimetal, and hexagonal boron nitride (hBN), an insulator, were grown on single-crystalline metallic substrates or a molten metal surface by ensuring an identical crystal orientation of all the grains to avoid any grain boundaries during coalescence (*18*–*22*). However, for 2D semiconductors grown on a single-crystalline substrate, although the film has essentially one crystallographic orientation, translational grain boundaries still exist because of the presence of imperfectly stitched domains (*23*, *24*).

To mitigate this problem, we devised a seamless epitaxial growth of a 2D-confined single crystal via the solid-to-solid phase transition and recrystallization process. Wafer-scale lateral extension of van der Waals (vdW) 2H molybdenum ditelluride ($MoTe_2$) semiconductor was triggered by a single nucleus deliberately implanted in the center of an amorphous insulating wafer. Single-crystalline 2H $MoTe_2$ with 100% 2D film coverage, excellent uniformity, and large size was grown, which can be further used as a template for rapid epitaxy in a vertical manner. Transistor arrays fabricated with the single-crystalline 2H $MoTe_2$ wafers showed high electrical performance, with excellent uniformity and 100% device yield. Our method opens up possibilities for future industrial implementation of vdW 2D semiconductors for next-generation nanoelectronics.

The synthesis processes of wafer-scale single-crystalline 2H $MoTe_2$ film is shown schematically in Fig. 1A. First, the Mo film (3 nm thick) deposited on the Si/SiO_2 wafer was tellurized with Te vapor to obtain a polycrystalline 1T′ $MoTe_2$ wafer (~10 nm thick) with existence of Te vacancies (see supplementary materials) (*25*, *26*). The domain size of the 1T′ $MoTe_2$ film was about tens of nanometers (fig. S1). After that, a single-crystalline 2H $MoTe_2$ nanoflake exfoliated from the bulk crystal was assembled to the center of the 1T′ $MoTe_2$ wafer by a dry transfer method (see supplementary materials) and served as a seed crystal to trigger the phase transition and recrystallization (Fig. 1, A and B).

Next, a 30-nm-thick dense Al_2O_3 layer was deposited on the surface of the wafer by atomic layer deposition (ALD) to isolate the 1T′ $MoTe_2$ film from the Te atoms in the environment during growth (Fig. 1A). Given that the supply of Te atoms for 1T′ $MoTe_2$ is a necessary condition for filling the Te vacancies to induce the 1T′ to 2H $MoTe_2$ phase transition (*25*, *27*, *28*), this structure avoided the spontaneous nucleation of 2H $MoTe_2$ with random crystal orientations in the 1T′ $MoTe_2$ film (fig. S2). The phase transition and atom rearrangement started from the seed region and extended outward during the entire growth period, which was crucial for the growth of wafer-scale single-crystalline film. Thus, a small hole was introduced into the seed region as the only channel for the supply of Te atoms (Fig. 1, A and inset of C); the hole was punched by a tungsten probe mounted on a 3D translation stage (fig. S3). The wafer and a 3-g Te lump (prepared by annealing Te powders at 500°C for 30 min) were placed in a closed quartz tube with a removable plug and then loaded into a 5-cm (2-inch) quartz tube in a chemical vapor deposition (CVD) furnace. This closed environment effectively reduced the consumption of Te sources, thereby ensuring the continuous supply of Te during the entire growth process. The wafer-scale single-crystalline 2H $MoTe_2$ film was synthesized at a flow rate of 5 standard cubic centimeters per minute (sccm) of Ar and 4 sccm of H_2 under atmospheric pressure.

The 1T′ $MoTe_2$ layer underneath the seed crystal transformed into a 2H $MoTe_2$ single crystal with the same crystallographic orientation as the seed crystal through the phase transition and recrystallization induced by the vertical 2H/1T′ interface (Fig. 1A). In this way, an in-plane 2H/1T′ $MoTe_2$ interface was formed, and the recrystallization and phase transition occurred at this interface and extended outward. The phase transition process was driven by atom diffusion, thus resulting in a single-crystalline 2H $MoTe_2$ circle centered on the seed region. At an intermediate stage of growth (650°C, 2 hours), we observed a 2H $MoTe_2$ circle with a radius of ~396 μm centered on the seed region (Fig. 1C), indicating that the phase transition rate was 3.3 μm/min under these conditions.

Before growth, both the typical Raman peaks of 2H (E_{2g}, 234 cm^{-1}) and 1T′ (A_g, 161 cm^{-1}; and A_g, 256 cm^{-1}) $MoTe_2$ could be observed in the

[1]State Key Laboratory for Mesoscopic Physics and Frontiers Science Center for Nano-Optoelectronics, School of Physics, Peking University, Beijing 100871, China. [2]Collaborative Innovation Center of Quantum Matter, Beijing 100871, China. [3]Electron Microscopy Laboratory, School of Physics, Peking University, Beijing 100871, China. [4]International Center for Quantum Materials, School of Physics, Peking University, Beijing 100871, China. [5]State Key Laboratory of Quantum Optics and Quantum Optics Devices, Institute of Opto-Electronics, Shanxi University, Taiyuan 03006, China. [6]Collaborative Innovation Center of Extreme Optics, Shanxi University, Taiyuan 03006, China. [7]Peking University Yangtze Delta Institute of Optoelectronics, Nantong 226010, Jiangsu, China.
*Corresponding author. Email: ye_yu@pku.edu.cn

Downloaded from https://www.science.org on September 04, 2023

Fig. 1. Seeded growth of the single-crystalline 2H $MoTe_2$ wafers. (**A**) The schematic diagrams for the in-plane 2D-epitaxy synthesis of wafer-scale single-crystalline 2H $MoTe_2$ thin film. (**B**) Optical image of a 2H $MoTe_2$ nanoflake assembled in the center of the 1T′ $MoTe_2$ wafer as a seed to induce the phase transition and recrystallization. (**C**) Optical image of the wafer after intermediate growth at 650°C for 2 hours. Inset shows the seed crystal with a needle probe–punched hole. (**D**) Raman spectra of the seed region before and after growth. a.u., arbitrary units. (**E**) Optical image of a synthesized 2.5-cm (1-inch) single-crystalline 2H $MoTe_2$ wafer.

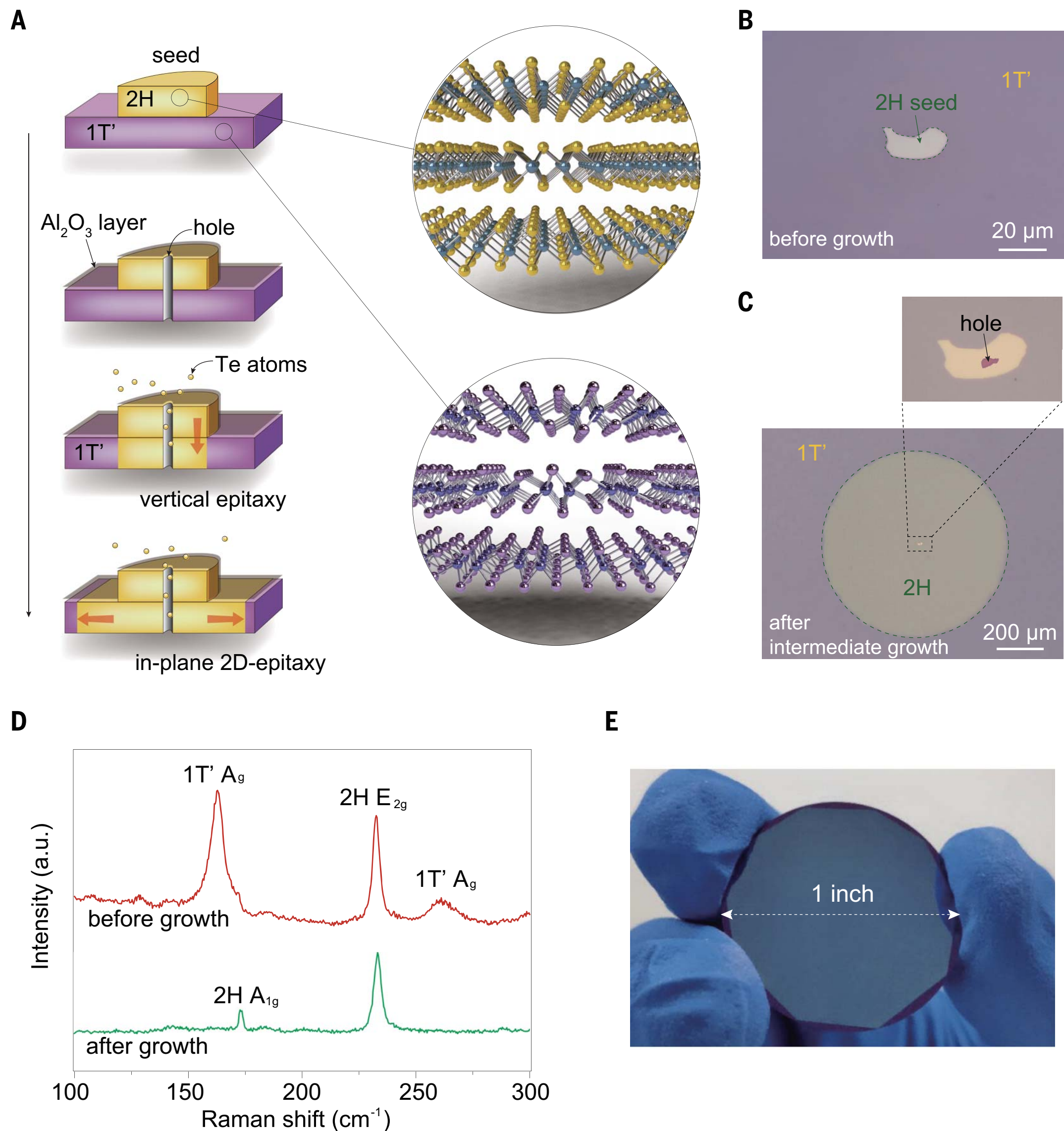

Downloaded from https://www.science.org on September 04, 2023

seed region (Fig. 1D) (*29*, *30*). After growth, only the Raman peak of 2H $MoTe_2$ was observed (Fig. 1D), indicating that the implanted seed induced the phase transition of 1T′ $MoTe_2$ at the bottom into 2H $MoTe_2$ (Fig. 1A). The vertical 2H/1T′ $MoTe_2$ interface was the key factor, in that other 2D materials (such as graphene and hBN) could not be used as the seeds to induce the phase transition of the 1T′ $MoTe_2$ at the bottom (fig. S4). Initial 1T′ $MoTe_2$ film of 2 to 3 nm was discontinuous and had a surface roughness, R_a, of ~1.2 nm, while the film of 35.5 nm became very rough with a R_a of ~3.7 nm. The film discontinuity and roughness resulted in a poor interface between the seed and the 1T′ film, which prevented the film under the seed region from phase transition through the vertical interface. Under all other initial 1T′ $MoTe_2$ film thicknesses, the seed-induced phase transitions were observed (figs. S5 and S6). After 3 days of long-term growth, the entire film phase-transformed into the 2H phase to form a wafer-scale semiconducting $MoTe_2$ single crystal with a diameter of 2.5 cm (1 inch) (Fig. 1E). The obtained film was continuous, smooth, and uniform over a large scale, with an R_a in the range of 0.20 to 0.25 nm (figs. S7 and S8). As long as the growth condition remained unchanged, the growth rate was relatively stable over time (fig. S9). At a temperature below 530°C, no phase transition occurred, because such a low temperature could not provide sufficient energy to cross the activation barrier of the phase transition (*25*). At temperatures above 710°C, the film was destroyed. Under all other temperatures, the seed-induced phase transition occurred, with a phase transition rate increasing exponentially with increasing temperature (fig. S10). The first-principle calculation and designed experiments confirmed that the diffusion rate of Te atoms was faster than the recrystallization rate, indicating that the phase transition rate was limited by the recrystallization rate under our growth conditions (figs. S11 and S12).

We used aberration-corrected scanning transmission electron microscopy (AC-STEM) to evaluate the crystallinity of the film around the seed region (Fig. 2A). The high-angle annular dark-field (HAADF) image of the thicker seed region, which appeared brighter owing to the larger sample thickness (*31*), showed a hexagonal lattice structure without any moiré patterns (Fig. 2C). The results showed that the lattice structure, orientation, and stacking order of the bottom $MoTe_2$ were exactly the same as those of the seed crystal. The Te and Mo atoms in the bottom 1T′ $MoTe_2$ rearranged according to the lattice structure of

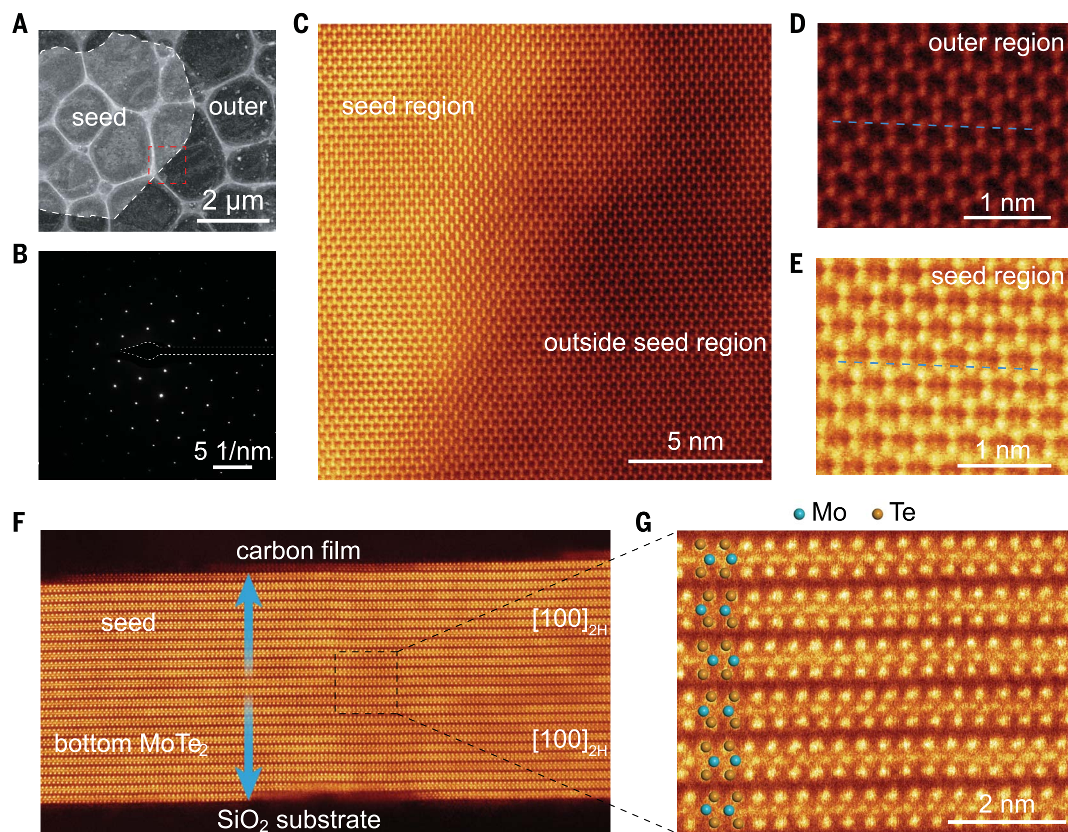

Fig. 2. TEM characterization around the seed region. (**A**) Low-magnification STEM image of the single-crystalline $MoTe_2$ film. The outline of the seed is marked by the dashed white line. (**B**) SAED pattern obtained at an area around the edge of the seed [marked by the dashed red box in (A)], containing only one set of sixfold symmetric 2H phase spots. (**C**) HAADF-STEM image acquired around the edge of the seed. (**D** and **E**) The zoomed-in STEM image of the seed region and the outside seed region, sharing the same crystal structure and orientation. The blue dashed lines indicate the zigzag crystal direction of 2H $MoTe_2$. (**F** and **G**) The cross-sectional HAADF-STEM image and zoomed-in image of the seed region.

2H $MoTe_2$ at the vertical 2H/1T′ interface during the phase transition. This recrystallization behavior was confirmed by the cross-sectional STEM characterizations of the seed region. Both the seed and bottom $MoTe_2$ layer maintained a perfect AB stacking order and had exactly the same crystal orientation (Fig. 2F), and there was no obvious gap between the seed and bottom $MoTe_2$ layers (Fig. 2G). The outside seed region also showed the hexagonal lattice structure of the 2H $MoTe_2$ (Fig. 2C), and its crystal orientation was the same as that of the seed region (Fig. 2, D and E), indicating that a similar recrystallization process also occurred during the in-plane phase transition.

During the phase transition, the Te and Mo atoms in the metastable 1T′ $MoTe_2$ migrated and rearranged themselves according to the lattice structure and orientation of the adjacent 2H $MoTe_2$ at the in-plane interface (*32*). Because this phase transition was driven by an atom-diffusion process in which the 2H $MoTe_2$ at the interface served as a template, the process was not substrate-sensitive and could even be performed on an amorphous SiO_2 surface. Thus, subsequent device fabrication could be performed directly on the substrate without the need to transfer the 2D semiconductor film, thus preserving the material quality and the integrity of the film. Owing to the 2D nature of the as-synthesized film, the intact 2D film wafer could also be transferred to other substrates (fig. S13). Because the as-synthesized films were multilayered, an atomic defect might not be visible in the Z-contrast image, because of the presence of other atoms from all other layers that could obscure the slight changes in the column intensity (fig. S14). In principle, the phase transition occurred from the Te vacancy–related 1T′ $MoTe_2$ phase to the stoichiometric 2H $MoTe_2$ phase, and this phase transition process did not suffer from the difficulty of balancing metal and chalcogen vapor pressures as other transition metal dichalcogenides (TMDCs) during the growth (*33*). From the energy dispersive x-ray spectroscopy (EDX) spectrum of the obtained film with a size of 300 nm by 300 nm (fig. S14), no corresponding peaks related to Si and Al were observed, indicating that Si and Al were not incorporated into the 2H $MoTe_2$ film during the high-temperature growth. The selected area electron diffraction (SAED) pattern obtained around the seed region (marked with the red dashed box in Fig. 2A) contained only one set of sixfold symmetrical 2H phase spots (Fig. 2B), further confirming that bottom and nearby $MoTe_2$ of the seed region inherited the lattice structure and crystal orientation of those of seed 2H $MoTe_2$.

We used electron back-scattered diffraction (EBSD) to further analyze the crystallinity of the film on a large length scale. The scanning electron microscope (SEM) image of a representative seed with a hole is shown in Fig. 3A. In the inverse pole figure (IPF) map along the normal direction of the surface (fig. S15), the uniform red color (related to the [0001] crystal orientation) indicated that the 2H $MoTe_2$ layers were stacked along the normal direction, which was consistent with cross-sectional STEM results. The in-plane transverse IPF map showed a uniform green color (Fig. 3B), indicating that the in-plane crystal orientation of the film around the seed region was the same, which was again consistent with the STEM results at a larger scale. Because the phase transition gradually advanced outward through the 2H/1T′ interface, the phase transition is thorough on the entire wafer. The obtained 2H phase film was continuous with 100% coverage, as confirmed by the uniform color of the phase-distribution map (Fig. 3C) related to the 2H phase. We also performed EBSD characterization of a larger area (1 mm by 1 mm) far away from the seed (marked by the green box in Fig. 3D). The in-plane IPF map showed not only a single color but also exactly the same color as that of the seed region (Fig. 3E), confirming that after the phase transition, the entire film strictly inherited the crystal lattice and orientation of the seed.

To further verify the single crystallinity, electron back-scattered patterns (EBSPs) were

Downloaded from https://www.science.org on September 04, 2023

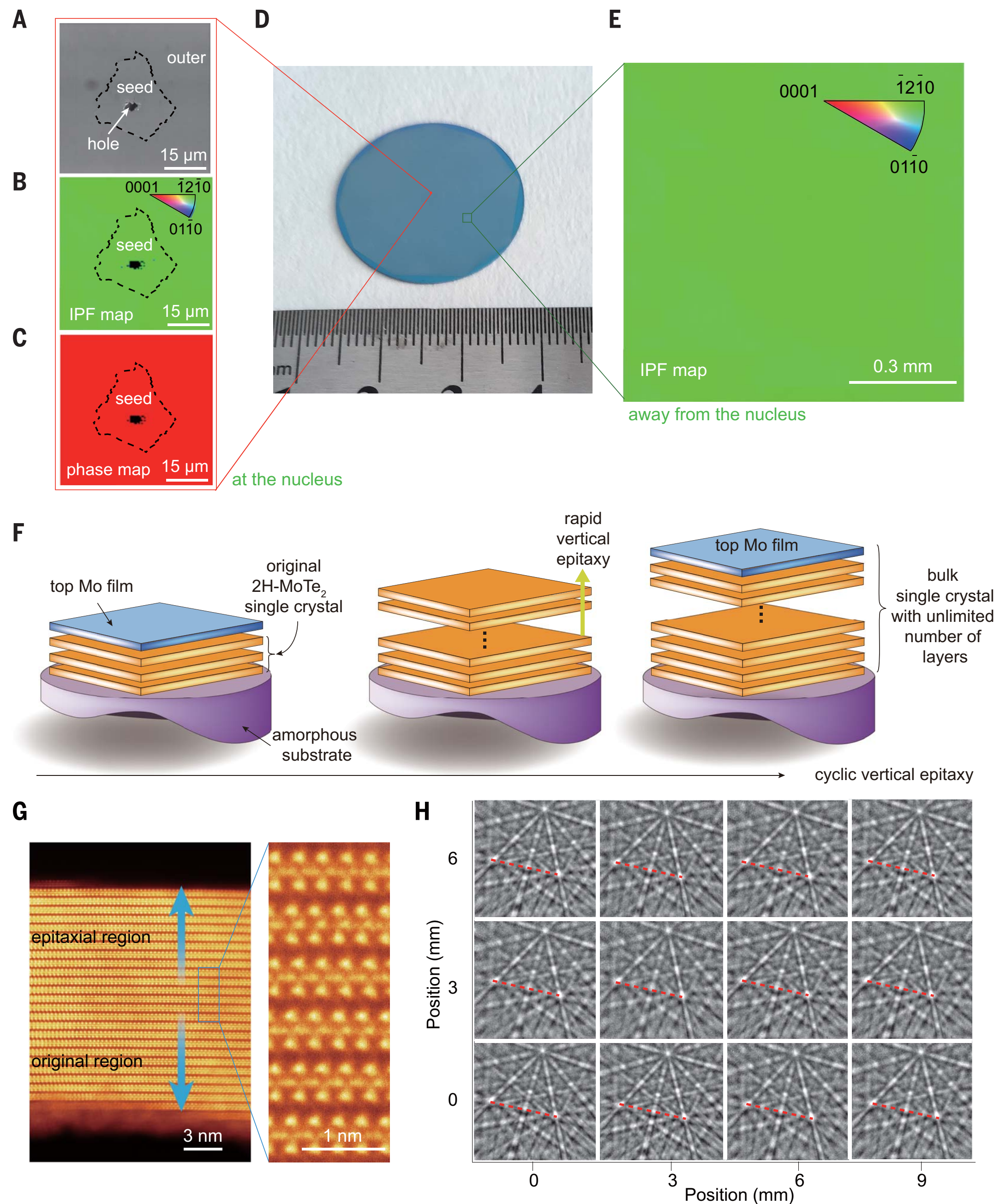

Fig. 3. EBSD characterization of the wafer-scale single-crystalline $MoTe_2$. (**A**) SEM image around the seed region. The outline of the seed with a hole at the center was marked by the dashed black line. (**B**) The in-plane transverse IPF map showed a uniform green color, confirming that the in-plane crystal orientation was identical at the region around the seed. (**C**) The phase distribution map at the same region as that of IPF map. (**D**) Optical image of the 2.5-cm (1-inch) single-crystalline $MoTe_2$ wafer. (**E**) The in-plane transverse IPF map of a large area far away from the seed. (**F**) The schematic diagrams of the cyclic rapid vertical epitaxy of the single crystal into a bulk single crystal with an unlimited number of layers. (**G**) The cross-sectional HAADF-STEM images of the epitaxial film. (**H**) EBSPs at different positions across the wafer.

Downloaded from https://www.science.org on September 04, 2023

randomly collected at different positions across the 2.5-cm (1-inch) wafer. All EBSPs showed only one set of Kikuchi patterns (related to the 2H $MoTe_2$) and had the same crystal orientation (fig. S16). The EBSP analysis unambiguously demonstrated that the wafer film was a single crystal whose crystal orientation was completely determined by the implanted seed crystal. If the crystal orientation of the seed crystal was deformed, the deformation was inherited throughout the film (fig. S17). This effect could provide a method for controllably preparing grain boundaries with different angles. In some cases, with an imperfect seed, we found that the IPF maps of the obtained $MoTe_2$ films showed small angle deflections (usually less than 1°) radiating from the seeds (fig. S18). These deflections might be caused by the stress generated during the seed-transfer process or stress caused by thermal fluctuations during growth.

Rapid epitaxy in the stacking direction using the single-crystalline 2H $MoTe_2$ 2D semiconductor single-crystal bulk wafer, as shown schematically in Fig. 3F. First, the Al_2O_3 film on the single-crystalline 2H $MoTe_2$ wafer was dissolved using a hot phosphoric acid solution (see materials and methods). A Mo film (3 nm thick) was deposited on the wafer. Then, the wafer was sent back into the furnace for tellurizing at 650°C for 5 min. The Mo film was initially converted into 1T′ $MoTe_2$ and formed a vertical 2H/1T′ $MoTe_2$ interface. Phase transition and recrystallization were induced through the interface. Similar to the seed-induced recrystallization discussed above, in a short period of time, the Te and Mo atoms in the top 1T′ $MoTe_2$ migrated and rearranged according to the lattice structure and orientation of the bottom wafer-scale single-crystalline 2H $MoTe_2$, thereby achieving the rapid epitaxy of

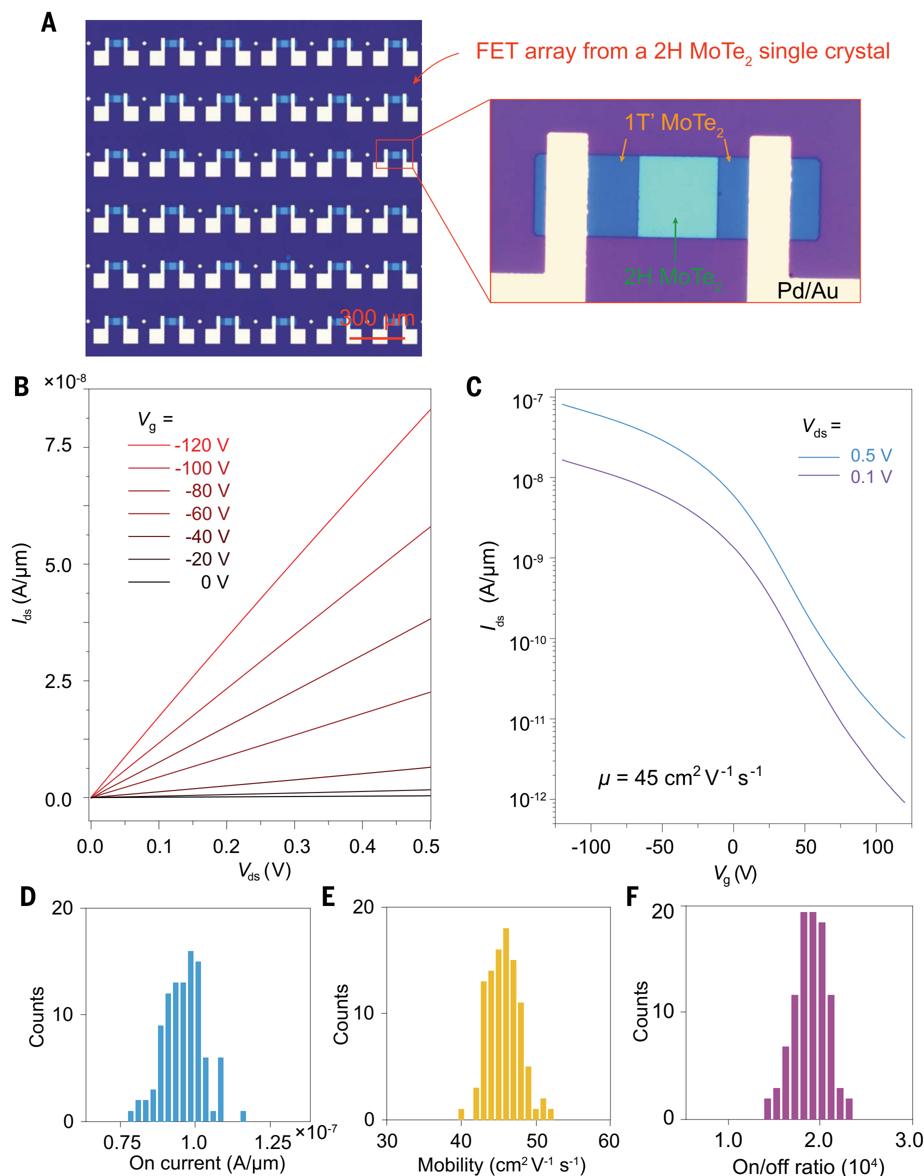

Fig. 4. Electrical characterizations of the FET devices fabricated on the single-crystalline 2H $MoTe_2$ film. (**A**) Optical image of the heterophase 1T′/2H/1T′ $MoTe_2$ FET array fabricated with a phase-engineered method. (**B**) Typical I_{ds}-V_{ds} curves of heterophase FET measured under various gate voltages. (**C**) Typical transfer curves of the heterophase FET. (**D** to **F**) The statistical histograms of the on-current, field-effect mobility, and on/off ratio measured on a 10 by 10 $MoTe_2$ FET array, all showing a narrow distribution.

Downloaded from https://www.science.org on September 04, 2023

the wafer. The thickness of the film increased from 10 to 20 nm after the epitaxy (fig. S19), indicating that both the original and epitaxial films are about 14 layers thick.

The single crystallinity of the film was characterized by STEM and EBSD. The cross-sectional HAADF-STEM image showed that the films in both the original and epitaxial regions maintained a perfect AB stacking order, and there was no observable gap between the original and epitaxial layers (Fig. 3G). The top-view HAADF-STEM image and the SAED pattern (fig. S20) showed a pure hexagonal lattice and a set of sixfold symmetric diffraction spots, respectively, indicating that an atomic-precision epitaxy of the 2H $MoTe_2$ was realized. EBSPs were also collected at different positions across the wafer. All EBSPs showed one set of 2H $MoTe_2$ Kikuchi patterns with the same crystal orientation (Fig. 3H), indicating that the epitaxy was consistent throughout the sample scale. The number of epitaxial layers was determined by the thickness of the deposited Mo film, and the epitaxy speed exceeded 150 layers per hour. This vertical epitaxy process could also be repeated as long as there is a single-crystal template. The rapid epitaxy method could be used in combination with the recently reported wafer-scale single-layer 2D materials peeling technique (*34*) to mass-produce single-layer single-crystalline 2H $MoTe_2$ wafers.

For monolithic integration technology, high device uniformity and reliability are critical, and we expected that the uniformity and reliability of the device could be greatly improved with single-crystalline films. On the basis of the wafer-scale single-crystalline 2H $MoTe_2$ thin film and our previously developed phase-engineered growth technique (see materials and methods for details) (*35*), we fabricated a large-scale coplanar heterophase 1T′/2H/1T′ $MoTe_2$ field-effect transistor (FET) array with optimized contacts directly on the growth substrate (Fig. 4A), with p^+-Si as the global back gate electrode. The typical gate voltage (V_g)–dependent source-drain current-voltage (I_{ds}-V_{ds}) output curves showed a linear response (Fig. 4B), indicative of a low contact barrier between the 1T′ and 2H $MoTe_2$ (fig. S21). The typical I_{ds}-V_g transfer curves at bias voltages of 0.5 and 0.1 V showed p-type transistor characteristics (Fig. 4C). From the transfer characteristics, we extracted a room-temperature field-effect mobility (μ) of ~45 $cm^2 V^{-1} s^{-1}$ and an on/off ratio of ~1.5×10^4 (Fig. 4C), comparable to the reported values of single-crystalline 2H $MoTe_2$

nanoflake transistors with a similar in-plane heterophase structure (*36*, *37*). Moreover, the channel could be fully turned off when measured in vacuum, showing an enhanced on/off ratio of $\sim 2 \times 10^6$ (fig. S22), because adsorbed gas molecules (such as oxygen and water) in ambient could induce a conducting channel near the top surface that could not be fully turned off by the back gate (*38*, *39*). The temperature-dependent Hall measurements confirmed that the mobility was limited by the phonon-related scattering, indicating the high electrical performance of the obtained 2H $MoTe_2$ film (fig. S23). The statistical results of the 10 by 10 $MoTe_2$ FET array showed that the on-current, field-effect mobility, and on/off ratio of the device were all highly narrow-distributed, with an average value of $9.38 \pm 0.75 \times 10^{-8}$ A/μm, 45 ± 2 cm^2 V^{-1} s^{-1}, and $1.8 \pm 0.3 \times 10^4$, respectively (Fig. 4, D to F), confirming the spatial uniformity of the electrical properties of the devices on a large scale. The single-crystalline nature of the continuous film also ensures a 100% device yield.

Until now, applying this method to other TMDCs required more effort, because the energy differences between the 2H phase and 1T′/1T phase of other TMDCs are much larger than that of $MoTe_2$. But big strides have been achieved in the synthesis of the 1T/1T′ phase of other TMDCs. For example, the stable 1T′ phase of MoS_2 has been synthesized directly using a CVD method by choosing the proper precursor of K_2MoS_4 (*40*). The high phase-purity 1T′ MoS_2 and $MoSe_2$ have also been synthesized by the mixture of K_2MoS_4 with S and Se (*41*). Meanwhile, the transition from the 1T′ phase to the 2H phase is observed by thermal annealing and laser irradiation. With the development of phase-engineering techniques, this method might be applied to other 2D materials. As in silicon manufacturing, the electrical characteristics of the semiconducting 2H $MoTe_2$ wafers can be controlled by adding dopants such as Nb and Re to the Mo film before it is tellurized. The ability to use this method on a variety of substrates might lead to the widespread adoption of 2D semiconductors in conventional CMOS devices.

REFERENCES AND NOTES

1. B. Radisavljevic, A. Radenovic, J. Brivio, V. Giacometti, A. Kis, *Nat. Nanotechnol.* **6**, 147–150 (2011).
2. L. Li *et al.*, *Nat. Nanotechnol.* **9**, 372–377 (2014).
3. S. B. Desai *et al.*, *Science* **354**, 99–102 (2016).
4. S. Manzeli, D. Ovchinnikov, D. Pasquier, O. V. Yazyev, A. Kis, *Nat. Rev. Mater.* **2**, 17033 (2017).
5. K. F. Mak, J. Shan, *Nat. Photonics* **10**, 216–226 (2016).
6. D. A. Bandurin *et al.*, *Nat. Nanotechnol.* **12**, 223–227 (2017).
7. C. Liu *et al.*, *Nat. Nanotechnol.* **15**, 545–557 (2020).
8. G. Fiori *et al.*, *Nat. Nanotechnol.* **9**, 768–779 (2014).
9. C. Liu, L. Wang, J. Qi, K. Liu, *Adv. Mater.* **32**, e2000046 (2020).
10. J. Dong, L. Zhang, F. Ding, *Adv. Mater.* **31**, e1801583 (2019).
11. C. Zhao *et al.*, *Nat. Nanotechnol.* **15**, 53–58 (2020).
12. K. Kang *et al.*, *Nature* **550**, 229–233 (2017).
13. K. Kang *et al.*, *Nature* **520**, 656–660 (2015).
14. Q. Wang *et al.*, *Nano Lett.* **20**, 7193–7199 (2020).
15. D. Rhodes, S. H. Chae, R. Ribeiro-Palau, J. Hone, *Nat. Mater.* **18**, 541–549 (2019).
16. J. Zhou *et al.*, *Nature* **556**, 355–359 (2018).
17. H. Lin *et al.*, *Nat. Mater.* **18**, 602–607 (2019).
18. T.-A. Chen *et al.*, *Nature* **579**, 219–223 (2020).
19. L. Wang *et al.*, *Nature* **570**, 91–95 (2019).
20. V. L. Nguyen *et al.*, *Nat. Nanotechnol.* **15**, 861–867 (2020).
21. X. Xu *et al.*, *Sci. Bull.* **62**, 1074–1080 (2017).
22. J. S. Lee *et al.*, *Science* **362**, 817–821 (2018).
23. D. R. Hickey *et al.*, arXiv:2006.11668 [cond-mat.mtrl-sci] (20 June 2020).
24. M. Chubarov *et al.*, arXiv:2006.10952 [cond-mat.mtrl-sci] (19 June 2020).
25. X. Xu *et al.*, *J. Am. Chem. Soc.* **141**, 2128–2134 (2019).
26. L. Zhou *et al.*, *J. Am. Chem. Soc.* **137**, 11892–11895 (2015).
27. J. C. Park *et al.*, *ACS Nano* **9**, 6548–6554 (2015).
28. X. Zhu *et al.*, *J. Mater. Chem. C* **7**, 10598–10604 (2019).
29. M. Yamamoto *et al.*, *ACS Nano* **8**, 3895–3903 (2014).
30. R. Beams *et al.*, *ACS Nano* **10**, 9626–9636 (2016).
31. O. L. Krivanek *et al.*, *Nature* **464**, 571–574 (2010).
32. X. Xu *et al.*, *Adv. Mater.* **32**, e2000236 (2020).
33. D. Edelberg *et al.*, *Nano Lett.* **19**, 4371–4379 (2019).
34. J. Shim *et al.*, *Science* **362**, 665–670 (2018).
35. X. Xu *et al.*, *Nano Lett.* **19**, 6845–6852 (2019).
36. S. Cho *et al.*, *Science* **349**, 625–628 (2015).
37. J. H. Sung *et al.*, *Nat. Nanotechnol.* **12**, 1064–1070 (2017).
38. A. J. Arnold, D. S. Schulman, S. Das, *ACS Nano* **14**, 13557–13568 (2020).
39. N. R. Pradhan *et al.*, *ACS Nano* **8**, 5911–5920 (2014).
40. L. Liu *et al.*, *Nat. Mater.* **17**, 1108–1114 (2018).
41. Y. Yu *et al.*, *Nat. Chem.* **10**, 638–643 (2018).

ACKNOWLEDGMENTS

Funding: This work was supported by the National Key R&D Program of China (grants 2018YFA0306900 and 2017YFA0206301), the Beijing Natural Science Foundation (4182028), the China Postdoctoral Science Foundation (2020TQ0015), the Key Research Program of Frontier Sciences, CAS (grant ZDBS-LY-JSC015), the National Natural Science Foundation of China (grants 61521004 and 11974024), and the Strategic Priority Research Program of the Chinese Academy of Science (grant XDB33000000). We are grateful for computational resources provided by Peking University, the TianHe-1A supercomputer, and the Shanghai Supercomputer Center. **Author contributions:** Y.Y. and X.X. conceived of the project and designed the experiments. X.X. synthesized the film, characterized the film, fabricated the devices, and performed the electrical measurements. Y.Pa. and S.Liu assisted in the synthesis of the thin film and the fabrication of the devices. B.H. conducted the STEM and EDX characterizations under the direction of P.Ga. W.X. performed the magnetron sputtering. P.Gu. performed the temperature-dependent electrical measurements. S.Li conducted the DFT calculations under the direction of J.C. Z.H. and Y.Pe. provided useful discussions. Y.Y. supervised this research. X.X. and Y.Y. wrote the manuscript. All authors contributed to discussions. **Competing interests:** None declared. **Data and materials availability:** All data needed to evaluate the conclusions in this paper are present in the paper or the supplementary materials.

SUPPLEMENTARY MATERIALS

science.sciencemag.org/content/372/6538/195/suppl/DC1
Materials and Methods
Figs. S1 to S23
References (*42*–*47*)

4 November 2020; accepted 4 March 2021
10.1126/science.abf5825

Downloaded from https://www.science.org on September 04, 2023

Seeded 2D epitaxy of large-area single-crystal films of the van der Waals semiconductor 2H $MoTe_2$

Xiaolong Xu, Yu Pan, Shuai Liu, Bo Han, Pingfan Gu, Siheng Li, Wanjin Xu, Yuxuan Peng, Zheng Han, Ji Chen, Peng Gao, and Yu Ye

Science, **372** (6538), .
DOI: 10.1126/science.abf5825

Seeding 2D crystals
Small, single crystals are often used to direct the growth of larger, bulk single crystals. Xu *et al.* modified these methods to grow single-crystal films of a two-dimensional (2D) semiconductor, 2H molybdenum ditelluride (2H $MoTe_2$), on an amorphous glass surface. After coating the wafer with a 1T# $MoTe_2$ film, a small 2H $MoTe_2$ crystallite was placed on the wafer. The wafer was capped with an alumina film, except for a small hole above the seed region that allowed entry of additional tellurium during the heating process that drove the phase transition and epitaxial growth of 2H $MoTe_2$.

Science, this issue p. 195

Downloaded from https://www.science.org on September 04, 2023

View the article online
https://www.science.org/doi/10.1126/science.abf5825
Permissions
https://www.science.org/help/reprints-and-permissions

Use of this article is subject to the Terms of service

Science (ISSN 1095-9203) is published by the American Association for the Advancement of Science. 1200 New York Avenue NW, Washington, DC 20005. The title *Science* is a registered trademark of AAAS.
Copyright © 2021 The Authors, some rights reserved; exclusive licensee American Association for the Advancement of Science. No claim to original U.S. Government Works